Dalton Transactions

ARTICLE TYPE

Novel enhanced visible-light-driven photocatalyst via hybridization of nanosized BiOCl and graphitic C$_3$N$_4$

Liwen Lei,[a,b] **Huihui Jin,**[a] **Qi Zhang,**[a] **Jun Xu,**[a] **Da Gao**[a] **and Zhengyi Fu**[b*]

Nanosized C$_3$N$_4$/BiOCl composites was synthesized via a facile method in the presence of arabic gum. Arabic gum acts as the structure-directing agent and helps the formation of BiOCl nanoparticles. A significant enhanced 10 **photodegradation is observed and a possible mechanism is proposed by combing photosensitization and photocatalyst.**

1. Introduction

Semiconductor photocatalysis have attracted a great deal of attentions as an effective way for organic pollutant remediation 15 and the conversion of solar energy into chemical energy. Although it is very effective under near-UV light irradiation with wavelength less than 387.5 nm, conventional TiO$_2$ photocatalyst is not ideal for application because it performs rather poorly in the processes associated with natural sunlight photocatalyst, 20 which is induced by its wide band gap (3-3.2eV). Considering that most solar light sources include plenty of visible light, the narrow optical absorption range of photocatalyst and low solar energy conversion efficiency are the major problems limiting the energy efficiency. Therefore, many efforts have been devoted to 25 developing more efficient and stable photocatalyst with good photogenerated charge separation as well as wide response wavelength range.[1,2]

In recent years, bimuth-based photocatalytic materials such as BiOX (X=Cl, Br, I), BiVO$_4$, BiWO$_6$ and Bi$_5$Nb$_3$O$_{15}$ etc. have 30 recently aroused great interest in the scientific community due to their intriguing electronic structures. Of these photocatalysts, BiOCl exhibits excellent photocatalytic activity to decompose organic compound into inorganic substances for purifying textile dye polluted waste water. Although BiOCl has a similar band gap 35 to TiO$_2$, but its layered structure endows it with the self-built internal static electric fields that can help the photoinduced hole-electron separation and the charge transport process, which promote the visible light photocatalytic activity.[3,4] Up to now, several efforts have been implemented to improve the activity of 40 the pristine catalyst by the control of morphology,[5,6] the selected orientation of crystal growth,[7] self-doping and surface modification.[8] However, it is still necessary to further improve the photocatalytic efficiency for practical applications.

One of the techniques for increasing the separation efficiency 45 of photogenerated hole-electron pairs is to form a hetero-structure photocatalyst using two kinds of semiconductors. Construction of hetero-structure by coupling two different semiconductors can help achieve the better separation of photoinduced electrons and holes and thus improve the photocatalytic efficiency dramatically. 50 Recently, to form hetero-structure by coupling with conjugative π structure materials has been extensively reported as an effective way to improve the photoinduced separation and a relatively slow charge recombination.[9-12]

Graphitic carbon nitride (g-C$_3$N$_4$) with nature of lamellar 55 structure can be readily synthesized by pyrolysis of many cheap nitrogen rich precursors.[13,14] This metal free semiconductor can form a π-conjugated plane and possess high thermal and chemical stability since the structure of g-C$_3$N$_4$ has the s-triazine ring with high condensation.[15] More important, g-C$_3$N$_4$ with a band gap of 60 2.7eV is chemically reactive in itself and was found to exhibit good photocatalytic activity for hydrogen production and organic pollution degradation under visible light irradiation. However, the photocatalytic performance of g-C$_3$N$_4$ is still limited for the high recombination rate of the photo-induced electron-hole pair. The 65 literature contains numerous reports related to g-C$_3$N$_4$ heterostructure catalysts,[16] such as ZnO/g-C$_3$N$_4$,[17] Bi$_2$WO$_6$/g-C$_3$N$_4$,[18] WO$_3$/g-C$_3$N$_4$[19] and BiOP$_4$/g-C$_3$N$_4$ [20]*etal*, which show the enhanced photocatalytic activities. Accordingly, g-C$_3$N$_4$ is an excellent component with π-conjugated structure to fabricating 70 the heterojunction catalysts to increase the photocatalytic activity of a semiconductor.

As a result, the combination of g-C$_3$N$_4$ with π-conjugated structure and BiOCl with open structure may be ideal system to achieve an enhanced charge separation. To our best knowledge, 75 very few reports focused on the synthesis of BiOCl coupling with g-C$_3$N$_4$ to highlight its photocatalytic performance. Very recently, Wang et al reported BiOCl photocatalysts hybridized with g-C$_3$N$_4$ prepared by using ionic liquid [HMIm]Cl as templates and the sources of Cl$^-$ to enhance the photocatalytic activities.[21] 80 Nevertheless, [HMIm]Cl is a little expensive and is harmful to environment. Herein, we firstly reported the synthesis of BiOCl and g-C$_3$N$_4$ heterostructured photocatalyst under mild condition. A nanoflower structured BiOCl was synthesized using arabic gum (AG) as template. AG is biopolymer gelatin as surface 85 protecting agent, which is known to contain many polar amino acids. The g-C$_3$N$_4$/BiOCl inorganic-organic hybrid photocatalysts showed superior photosensitized degradation activity of rhodamine B (RhB) to those of pure phases. The results showed that the addition of AG can improve evidently the specific surface 90 area of these hetero-structure catalysts and the interface condition which are vital to the photocatalytic performance of the hetero-

structure photocatalyst. Furthermore, among the heterostructure photocatalysts relating to BiOCl, the mechanism is rarely related to the photosensitization.[12,21-22] However, visible light with $\lambda>$ 420nm could not excite BiOCl because of its large band gap. Hence, the mechanism combining photosensitization with photocatalyst for the degradation of RhB over the g-C_3N_4/BiOCl photocatalysts was proposed.

2. Experimental

2.1 Catalysts preparation

All starting materials were guaranteed reagent and used without further purification. The g-C_3N_4 powder was prepared by direct polymerization of urea according to the literature.[23] In a typical synthesis run, 25g of urea was put into a semi-closed alumina crucible to prevent sublimation of precursors in a muffle furnace. The crucible was heated to 550℃ for 2h with a ramp rate of 2℃/min.. Next, 100mg of obtained yellow g-C_3N_4 powder dispersed in 100 mL of water, and then ultrasound for about 16h. The resulting suspension was centrifuged in low speed to remove the residual unexfoliated g-C_3N_4, followed by centrifugation at 10000rpm to obtain g-C_3N_4 nanosheets.

The typical preparation of nanosized g-C_3N_4/BiOCl photocatalysts was as follow: first, 0.1g AG was added into 100ml glycerol and stirred for 30min to dissolve AG completely. Then, the appropriate amount of g-C_3N_4 was completely dispersed into the saturated solution assisted by ultrasonication for 30min. After that, 0.45g KCl and 0.02mol carbamide was added into the above solution and stirred in a fume hood for another 30min. Next, 0.97g Bi(NO$_3$)$_3$·5H$_2$O was dissolved in it and stirred for an additional 60 min to get a stable, homogeneous precursor. Subsequently, the mixture was put into a water bath and heated at 80℃ for 12h. After fully reaction, the gained precipitate was collected and rinsed several times with deionized water and absolute ethanol respectively. Finally, the precipitate was dried at 60℃. According to this method, a series of C_3N_4/BiOCl photocatalysts with various g-C_3N_4 mass content of 0%, 5%, 10%, 20%, 30% and 100% were synthesized by this method and be denoted as BiOCl, 5C_3N_4/BiOCl, 10C_3N_4/BiOCl, 20C_3N_4/BiOCl, 30C_3N_4/BiOCl and g-C_3N_4 for convenience. In order to understand the role of AG in the synthesis of BiOCl and the composite, prisitine BiOCl and C_3N_4/BiOCl photocatalysts with 20% g-C_3N_4 mass content were prepared with the absence of AG under the same condition for comparison, which is assigned as BIOCL and 20C_3N_4-BiOCl respectively.

2.2 Characterization

Powder X-ray diffraction (XRD) patterns of the samples were obtained with a D/MAX-RB system with the Cu kα radiation from 10º to 80º with a step size of 0.02º. Morphological investigation was carried out with scanning electron microscopy (SEM, HITACHI-S3400N), field emission scanning electron microscopy (FESEM, HITACHI-S4800), transmission electron microscopy (TEM, Philips-CM12) and high-resolution transmission electron microscopy (HRTEM, JEOL-2010). X-ray photoelectron spectroscopy (XPS) measurements were performed on an ultrahigh-vacuum VG ESCALAB 210 electron spectrometer equipped with a multichannel detector. The spectra were excited using Mg KR (1253.6eV) radiation (operated at 200 W) of a twin anode in the constant analyzer energy mode with a pass energy of 30 eV. The charge effect was calibrated using the binding energy of C1s. UV–vis diffuse reflectance spectra (DRS) of the samples were recorded on a UV-2550 (Shimadzu) using BaSO$_4$ as the background. The Brunauer-Emmett-Teller (BET) surface area and pore size measurements were measured using nitrogen adsorption via a Micromeritics ASAP 2020 (USA) surface area analyzer. Fourier transform infrared (FTIR) spectra were acquired with a DTGS KBr detector using a Nicolet Nexus 670 spectrometer.

2.3 Photocurrent experiments

The electrochemical measurements were carried out on an electrochemical system (CHI600C, China). A standard three electrode system using the as-prepared samples as the working electrodes, a Pt wire as a counter electrode, and Ag/AgCl (saturated KCl) as a reference electrode were used in photoelectric studies. A 500W Xe acr lamp with a UV-cut off filter ($\lambda>$420 nm) served as a light source. 0.5M Na$_2$SO$_4$ aqueous solution was used the electrolyte. The working electrodes were FTO glass (0.5×1cm^2) coated with the as-prepared samples (5mg).

2.4 Photocatalytic experiments

Photocatalytic activities of the samples were evaluated by the decolorization of rhodamine B(RhB) under visible light irradiation at ambient temperature. A 500 W Xe-illuminator was used as a light source and set about 10 cm apart from the reactor. The 420 nm (or 532nm) cut-off filter was placed between the Xe-illuminator and the reactor to completely remove all incoming wavelengths shorter than 420 nm (or 532nm) to provide visible light. Experiments of RhB decolorization were carried out as follows: 10mg of photocatalyst powder was added to 100mL of 20mg L^{-1} RhB solution with constant stirring. Before illumination, the solutions were stirred for 1h in the dark to obtain adsorption-desorption equilibrium and eliminate the error due to any initial adsorption effect. At a given time intervals, about 5mL suspensions were collected, and centrifuged to separate the photocatalyst particles. The concentrations of the remnant RhB were then monitored by UV-vis spectrometer (Shimadzu UV-2550) at the wavelength of 553 nm.

The detection of active species in the photocatalytic reactivity is similar to the photodegradation experiment. Tert-butyl alcohol (t-BuOH), 1,4-benzoquinone (BQ) and ethylenediaminetetra acetic acid (EDTA-2Na) were selected to detect as hydroxyl radicals ($^\cdot$OH), superoxide radical (O$_2^{\cdot-}$)　and hole (h$^+$), respectively. 1mM scavenger was introduced into the RhB solution prior to addition of the photocatalyst. The detailed experiment process and the dosage of these scavengers were referred to the previous studies.[24]
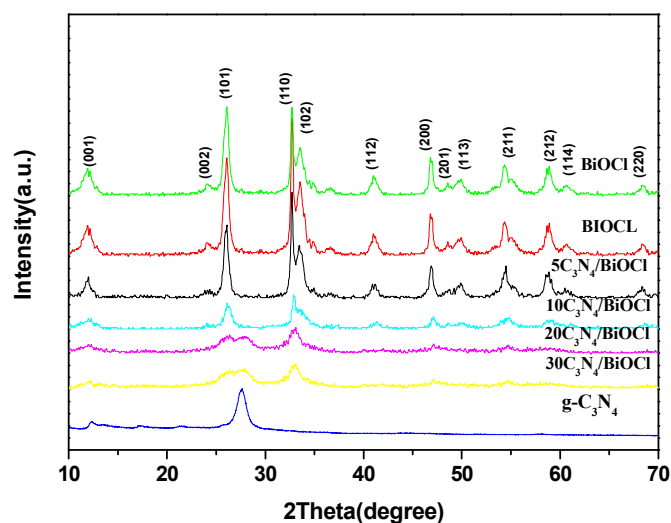
3. Results and discussions

Fig.1 XRD patterns of as-prepared photocatalysts in different compositions

3.1 Phase structures

Fig.1 shows the XRD profiles of g-C_3N_4, BiOCl, BIOCL and C_3N_4/BiOCl photocatalysts with different g-C_3N_4 mass content. As Fig.1a shown, two pronounce peaks are found in pristine g-C_3N_4 at 27.4º and 13.1º, which corresponds to the characteristic interplanar stacking of the conjugated aromatic system and the interlayer structural packing peak and can be indexed to (002) and (100) diffraction planes, respectively. Meanwhile, the diffraction peaks of BiOCl could be readily indexed to the tetragonal phase of BiOCl (JCPDS card no.06-0249). The XRD patterns of BIOCL are similar to those of BiOCl. It is worth noting that compared with BIOCL, the diffraction intensity ratio of (110)/(001) planes for BiOCl is relatively lower, which could be attributed to the smaller lateral size oriented along the [110] direction.[25,26]

The diffraction peaks of C_3N_4/BiOCl composite photocatalysts show that all the samples are well crystallized and the crystal phase of BiOCl does not change after the introduction of g-C_3N_4. No crystalline impurity phase is emerged in the C_3N_4/BiOCl photocatalysts. However, no characteristic g-C_3N_4 diffraction peak is observed with low g-C_3N_4 addition. With the increasing g-C_3N_4 content of the composite, the peaks assigned to g-C_3N_4 become stronger. Moreover, when the mass ratio of g-C_3N_4 is reached 30%, the intensity of the diffraction peaks of C_3N_4/BiOCl composite photocatalyst is decreased evidently compared to those with lower g-C_3N_4 mass content. During the synthetic processing, the nucleation and growth of BiOCl grains may preferentially occur on the surface of porous g-C_3N_4 sheets for the relatively lower nucleation energy of heterogeneous nucleation. The relative high content of g-C_3N_4 could wrap BiOCl grains and decrease the crystallinity of g-C_3N_4/BiOCl photocatalyst. Furthermore, it is apparent that no impurity phase is detected, confirming the high purity of g-C_3N_4/BiOCl photocatalysts.
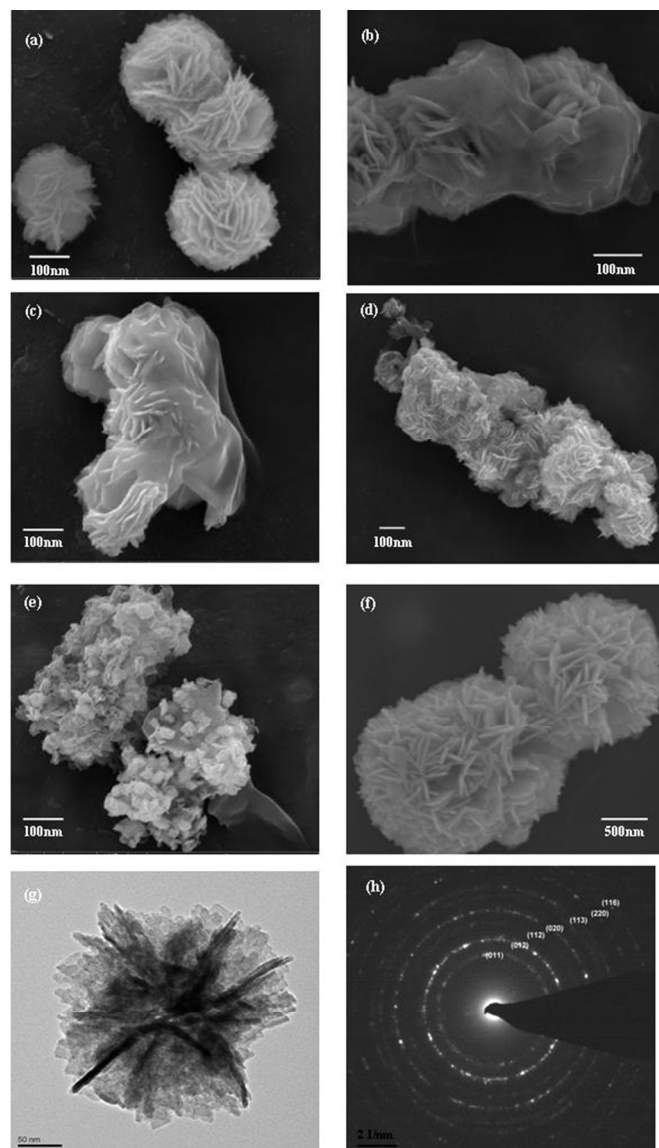
3.2 Morphology and surface area

Fig.2 SEM and images of (a) BiOCl (b) 5C_3N_4/BiOCl (c)10C_3N_4/BiOCl (d)20C_3N_4/BiOCl (e) 30C_3N_4/BiOCl (f) BIOCL and TEM images of (g) (h) BiOCl

The particle sizes and morphology of the representative photocatalysts were investigated by SEM and FESEM. Fig. 2a shows a typical SEM image of pristine BiOCl without g-C_3N_4. It is clear that the product exhibits homogenous flower-like nanostructure sphere with an average diameter of approximate 200nm. A TEM image of an individual pristine BiOCl particle, as shown in Fig 2g, clearly reveals that the flowerlike 3D hierarchical structure is constructed by many nanoflakes with thickness of around 5-8nm and a lateral size of about 100nm. The nanoflakes conglutinate at the centre and are composed of self-assembled nanoparticles. The ultrafine particles of BiOCl could be conducive to the coupling with g-C_3N_4 for the formation of hetero-structure photocatalyst due to the high surface energy. The detailed structures for BiOCl are further characterized by the selected-area electron diffraction (SAED) pattern (Fig. 2h) and show the continuous diffraction rings, revealing that the highly crystalline nature of the nano-flowers. It is worth noting that

BiOCl microstructures are highly sensitive to intensive electron beam irradiation, which was observed and reported in some groups.[27,28] The SEM picture of BIOCL in the absence of AG is shown in Fig. 2f. The shape of products is still flower-like sphere.

5 However, the size of the products size is far larger than BiOCl synthesized in the presence of AG. The above results are consistent with those of XRD and demonstrate further that the presence of AG plays a key role in the precipitation process being responsible for the formation of BiOCl particles with controlled

10 size. It is known that the isoelectric point of AG in aqueous solution is around 2.4. Hence, the AG molecules are expected to possess negative charges in this experimental reaction system at the pH value of 6.8. For the flower-like BiOCl, the single nano-sheet grows along the [110] direction and the side surfaces are

15 {110} facets. Then, the negative carboxylate charge groupings in AG are supposed to interact with {110} planes which enrich in Bi cations and suppress its growth. Therefore, the nanosheets of BiOCl in the presence of AG are shorter than those of BIOCL.

As seen from Fig.2b to Fig. 2d, BiOCl particles are well

20 wrapped by g-C_3N_4 sheets system and its shape has no significant change with relative low g-C_3N_4 amount. However, the regular flower-like shape may be disrupted with the increasing content of g-C_3N_4, which means that the excessive g-C_3N_4 in the reaction system can destroy the self-assemble processing of BiOCl. To

25 provide better insights into the morphology and microstructure of the as-prepared samples, TEM and HRTEM images of C_3N_4, 20C_3N_4/BiOCl are visualized in Fig.S1, EIS†. It is clearly seen that g-C_3N_4 (Fig.S1a) showed a two-dimensional slice-like structure with many pores and irregular shape, which is consistent

30 with the reference.[29] The BiOCl nanoflowers were wrapped by g-C_3N_4 sheets. The lattice fringes with interplanar distance corresponding to the XRD patterns are marked in Fig.S1(C), confirming the existence of C_3N_4 and BiOCl. The interplanar spacing value of 0.663nm in Fig. S1(C) corresponded to the (001)

35 planes of BiOCl, which means the lattice structure of BiOCl had no obvious change after the addition of g-C_3N_4. Smooth interfaces are found between BiOCl and C_3N_4. The specific surface area pore size distribution of as synthesized specimens were investigated by nitrogen adsorption-desorption analysis (as shown in Table1). It

40 can be found that the specific surface area of BiOCl is 49.51m^2/g, which is roughly equal to that of g-C_3N_4. Hence, the specific surface areas for the C_3N_4/BiOCl composites are the similar range

Table 1 Measured parameters for the specimens

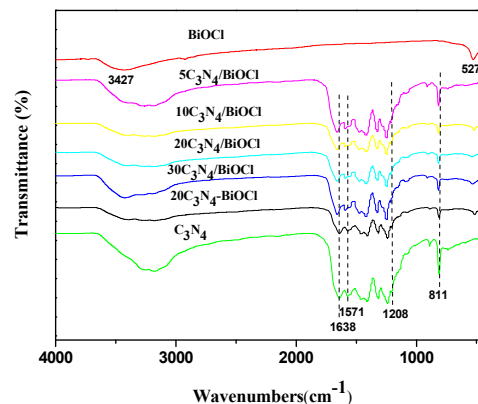| Samples name	Surface area ($m^2 g^{-1}$)	Kinetic rate constant(k) (min^{-1})	Adsorption capability (%)
g-C_3N_4	46.85	0.0078	9.2
BiOCl	49.51	0.1143	21.9
5C_3N_4/ BiOCl	48.82	0.1875	21.7
10C_3N_4/ BiOCl	50.47	0.1967	20.8
20C_3N_4/ BiOCl	49.37	0.3532	20.2
30C_3N_4/ BiOCl	51.03	0.1003	14.1
BIOCL	16.87	0.0871	17.7
20C_3N_4- BiOCl	32.16	0.1535	17.8

45

Fig. 3 FT-IR spectra of g-C_3N_4, BiOCl and C_3N_4/ BiOCl photocatalysts

from 45~51 m^2/g. However, BIOCL exhibits a relatively low specific surface area of 16.87 m^2/g. Therefore, AG acts as the structure-directing agent and help control the size of BiOCl

50 particles. The nano-sized BiOCl with higher specific surface area may favour the formation of intense interaction during the hybridization for the higher surface energy, producing more interfaces between g-C_3N_4 and BiOCl.

3.3 FT-IR spectroscopy analysis

55 Fig.3 displays a comparison of FT-IR spectra of g-C_3N_4, BiOCl, C_3N_4/BiOCl composites prepared in the presence of AG and 20C_3N_4-BiOCl prepared in the absence of a. In the FT-IR spectra of g-C_3N_4, the adsorption peak at 811cm^{-1} corresponds to the characteristic breathing mode of an s-triazine ring system. The

60 peak at 1638cm^{-1} is attributable to C=N stretching vibration modes, while the 1208-1571cm^{-1} are related to aromatic C–N stretching. The broad absorption band at 3100-3300cm^{-1} can be assigned to the stretching modes of secondary and primary amines and their intermolecular hydrogen-bonding interactions. Both of

65 the characteristic peaks of BiOCl (527cm^{-1}) and those of g-C_3N_4 were observed on C_3N_4/BiOCl photocatalysts, which means that the maintenance of the C_3N_4 and BiOCl structures during the hybridization. The characteristic peaks of g-C_3N_4 for 20C_3N_4-BiOCl do not move after combination with BiOCl nanoparticles.

70 Nevertheless, compared to 20C_3N_4-BiOCl photocatalyst, the red shift of all the main characteristic peaks belonging to g-C_3N_4 implies that the bond strengths of C=N and C–N would be attenuated. This phenomenon also appeared in the g-C_3N_4/ZnO and g-C_3N_4/ZnWO$_4$ systems, which means that the conjugated

75 system of C_3N_4 was stretched and a more widely conjugated system composed by g-C_3N_4 and BiOCl.[30,31] Furthermore, the intensity of the strong absorption peaks at 527cm^{-1} due to the Bi-O stretching mode is correlated with their concentration.[32]
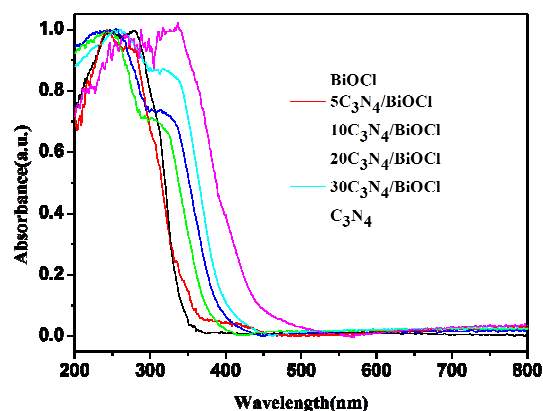
Fig.4 UV-Vis spectra of g-C_3N_4, BiOCl and C_3N_4/ BiOCl in different composition

3.4 Optical and photocatalytic properties

5 The optical properties of the specimens were studied using UV-vis spectrometer. As reviewed from Fig.4, the absorption edge of BiOCl is located at about 370nm while that of g-C_3N_4 is approximate to 460nm in the visible-light range. Based on the equation $(\alpha h\nu)^{2/n}=A(h\nu-E_g)$, where α, $h\nu$, A and E_g are,

10 respectively, the absorption coefficient, the photo energy, a constant and the optical band gap. In this equation, n is determined by the type of optical transition of a semiconductor (n=1 for direct transition and n=4 for indirect transition). According to the previous reports, the n values of BiOCl is 4 and that of g-C_3N_4 is

15 1.Thus, E_g of as-prepared BiOCl and g-C_3N_4 are estimated to 3.21 and 2.75eV, respectively. The UV-vis spectra of the C_3N_4/BiOCl composites can be seen as the overlap of the two components. Compared with that of BiOCl, the absorption edge of C_3N_4/BiOCl composites shows an apparent red shift due to the presence of g-

20 C_3N_4 on the BiOCl surface, which means the light response range of BiOCl is extended further in the visible region by the addition of g-C_3N_4. Additionally, the spectra range covered increases with the increase of g-C_3N_4 content, indicating the more production of electron-hole pairs and the higher photocatalytic performance.

25 In order to further determine the energy band structure of C_3N_4/BiOCl composites, the valence band (VB) and conduction band (CB) edge position of BiOCl and g-C_3N_4 are estimated by $E_{VB}=X-E^e+0.5E_g$, where E_{VB} is VB edge potential, X is the absolute electronegativity of the semiconductor, which is the

30 geometric mean of electronegativity of the constituent atoms, E^e is the energy of free electrons on the hydrogen scale (about 4.5eV). The CB edge potential can be obtained by $E_{CB}= E_{VB}-E_g$. Hence, the E_{VB} of g-C_3N_4 and BiOCl are 1.595 and 3.465eV, respectively. The E_{CB} of g-C_3N_4 and BiOCl are -1.155 and 0.255eV,

35 respectively.

3.5 Photocatalytic activity

The photocatalytic performances of all the as-prepared C_3N_4/BiOCl composites with different g-C_3N_4 concentration are evaluated by degradation of RhB which is chosen as the target
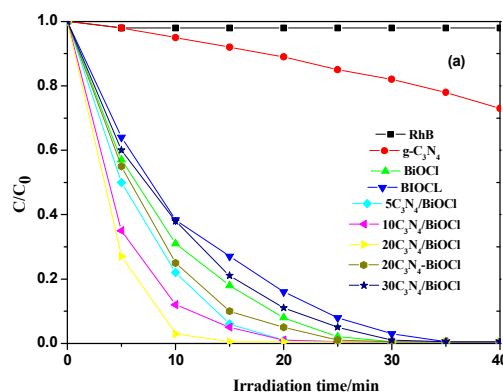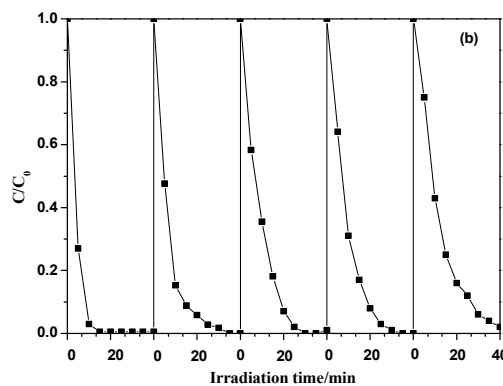

Fig.5 (a) Photodegradation of RhB over as-prepared photocatalyst (b)cyclic
45 photocatalytic degradation experiments of RhB by 20C_3N_4/ BiOCl composite photocatalyst

pollutant in aqueous solution by using 420nm UV cut off filter as light sources. Simply RhB photolysis was also performed for
50 comparison. As can be seen from Fig.5a, RhB can be rarely degraded under visible light illumination with the absence of photocatalyst, indicating that RhB is stable under experimental conditions. The degradation rate of RhB in the presence of BiOCl reaches 99.5% in 30 min while g-C_3N_4 only reaches 27% in
55 40min. Although BiOCl can not be activated by visible-light for its wide band gap, it shows superior degradation of RhB due to the self-sensitized degradation activity. To evaluate the photocatalytic efficiency quantitatively, the apparent photodegradation rate constants were obtained by fitting the lines of $\ln(C_0/C)$ vs. time.
60 The photocatalytic degradation of organic pollutants follows pseudo-first-order kinetic, and the value of apparent rate constant k were calculated and are shown in Table1. The introduction of appropriated amount of g-C_3N_4 could enhance the photocatalytic activity of BiOCl and the photocatalytic activity of C_3N_4/BiOCl
65 composites increases gradually with an increasing proportion of g-C_3N_4. When the content of g-C_3N_4 reached 20wt%, it exhibits the maximum photocatalytic activity. Then apparent rate constant k for 20 C_3N_4/BiOCl is 0.3532min^{-1}, which is about 3 times as high as that of BiOCl and 44 times that of g-C_3N_4. Further increase in
70 g-C_3N_4 concentration results in a significant decrease in the photocatalytic activity. When the content of g-C_3N_4 reaches 30wt%, the degradation rate is lower than that of BiOCl, but still higher than that of g-C_3N_4. Therefore, the composition ratio in
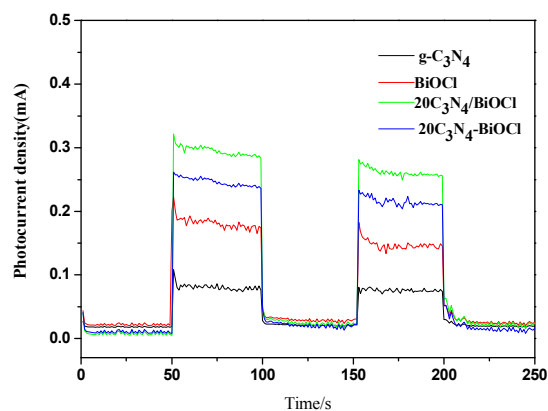
Fig.6 Transient photocurrent density versus time for g-C₃N₄, BiOCl, 20C₃N₄/BiOCl and 20C₃N₄-BiOCl photocatalysts

C₃N₄/BiOCl composites is pivotal for the demands of both the charge separation and light harvesting to achieve enhanced photocatalytic activity. The existence of optimal ratio for the photocatalyst composite is in agreement with the reports in the literatures,[27,28] which may be related to the synergetic effect between C₃N₄ and BiOCl. The suitable g-C₃N₄ content may favour it to bond with the BiOCl to produce more interfaces needed to allow the highly efficient interparticle charge transfer. In contrast, at much higher g-C₃N₄ content, the soft sheet-shaped g-C₃N₄ would covered more surface of BiOCl and shield visible light off of BiOCl and RhB due to the relative g-C₃N₄ higher content, inducing the decrease of photocatalytic activity. In addition, the adsorption of RhB is the crucial factor for photocatalyst. Accordingly, the poor activity of 30C3N4/BiOCl should also be attributed to the reduced adsorption of RhB (as shown in Table 1).

The influences of AG on the photocatalytic activities of C₃N₄/BiOCl composites are carried out, are also shown in Table 1. As seen in Table 1, the apparent rate constant of 20C₃N₄/BiOCl is nearly two faster than that of 20C₃N₄-BiOCl. The prominent photocatalytic performance of 20C₃N₄/BiOCl composite could be ascribed to two key points: the high adsorption capability toward the contaminant molecules and the cooperation of the components.[30] The adsorption capability was evaluated by the remaining concentration of the dye stirring in the dark in the presence of BiOCl until reaching the dye adsorption/desorption equilibrium. For BiOCl, the adsorption capability contributes more than the conduction band condition to the high photosensitized degradation rate.[26] The adsorption amounts of 20C₃N₄/BiOCl and 20C₃N₄-BiOCl toward different kind of dyes are shown in Fig.S2, EIS†. As expected, the adsorption of RhB over 20C₃N₄/BiOCl with larger specific surface area reaches 21.9%, which is higher than that of 20C₃N₄-BiOCl. Another possible reason related to the difference of adsorption capability may be related to the surface characteristics. The surface anionic sites will increase in the presence of AG, relying on the negative charge of AG. Generally, RhB dyes exist two forms: cationic form and zwitterionic form. However, RhB dyes in this system may be regarded as cationic due to the acidic environment. Therefore, they tended to be adsorbed on the negative charged surfaces. As a result, the adsorption capability of RhB of 20C₃N₄/BiOCl is larger than 20C₃N₄-BiOCl. To validate the above assumption, the
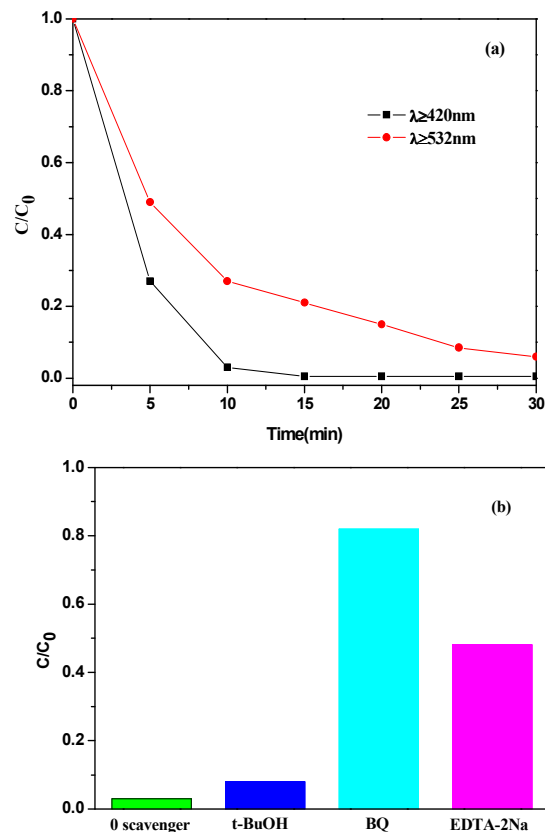

Fig.7 (a) Photodegradation of RhB over 20C₃N₄/BiOCl under different visible light irradiation (λ≥420 nm and λ≥532 nm) (b) Trapping experiment of active species for RhB degradation over 20C₃N₄/BiOCl under visible light irradiation

anionic dye MO is chosen as a model target dyes and the two composite photocatalysts toward MO are also shown in Fig.S3. Evidently, compared with RhB, the adsorption ability toward MO of 20C₃N₄/BiOCl is relative poor. In addition to the adsorption capability of dyes, the contact between the two components is also an important factor affecting the photocatalytic activity because the presence of the interface is needed to allow the highly efficient interparticle charge transfer.[33] The poor contact between the two semiconductors would retard the charge transfer and decrease the separation efficiency. Therefore, the prominent performance of 20C₃N₄/BiOCl could be also ascribed to the better cooperation of BiOCl and g-C₃N₄. As the results discussed above, the interface contact of 20C₃N₄/BiOCl is stronger than that of 20C₃N₄-BiOCl.Although the C₃N₄/BiOCl composites exhibit higher photocatalytic activity, considering the practice applications, the stability of the photocatalytic performance is also very important. The recycling experiments on 20C₃N₄/BiOCl were carried out for five times under the same reaction conditions to evaluate the stability of the composites (as shown in Fig.5b). It can be seen that the photocatalytic activity of 20C₃N₄/BiOCl is retained about 90% of its original activity after five cycles under visible light irradiation, indicating that its superior stability during photocatalyst. The kinetic rate constant (min⁻¹) Therefore, the C₃N₄/BiOCl composites have a promising practical application in
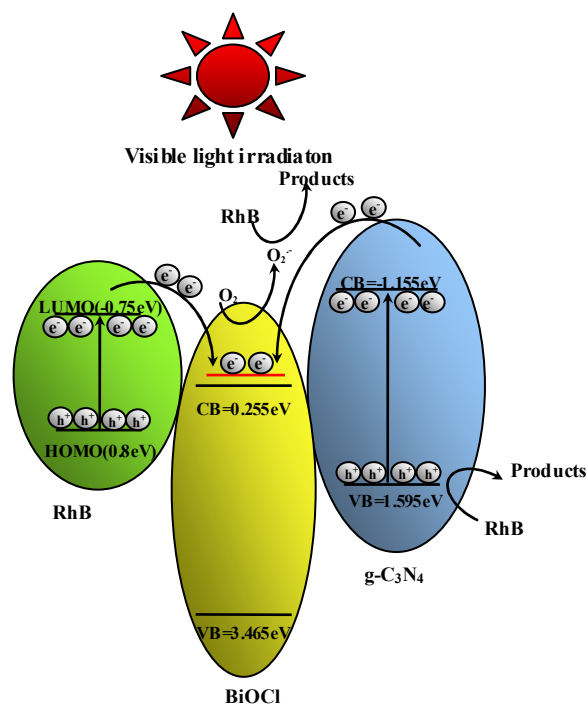
Scheme.1 The schematic diagram of charge separation and photocatalytic process of the C_3N_4/BiOCl photocatalysts under visible light irradiation

environmental protection originating from its high activity and stability.

3.6 Photocurrent-time measurements

Photocurrent-time measurements were performed to C_3N_4/BiOCl and BiOCl electrodes elucidate the interfacial charge transfer dynamics between the interfacial surface of the BiOCl and g-C_3N_4. Generally, the photocurrent is widely regarded as the most evidence demonstrating the charge separation for the photocatalysts. Fig.6 shows the transient photocurrent response of 20C_3N_4/BiOCl, 20C_3N_4-BiOCl, BiOCl and g-C_3N_4 measured by two on-and-off cycle mode of visible-light irradiation. It is obvious that the photocurrent response of both specimens switch reversibly and reproducibly when the visible light is turned on and off, indicating the high photophysical stability of the specimens. Furthermore, as can be seen from Fig.6, the photocurrent intensities of 20C_3N_4/BiOCl and 20C_3N_4-BiOCl are both higher than that of BiOCl and g-C_3N_4, indicating that more the longer living photoinduced carriers and the suppression of the charge recombination after the hybridization.[31] Noteworthy, 20C_3N_4/BiOCl photocatalyst presents the highest photocurrent intensity and still higher than that of 20C_3N_4-BiOCl, demonstrating that a lower recombination and a more efficient separation of photoinduced electron-hole pairs for hybrid at the 20C_3N_4/BiOCl interfaces. The results are consistent with photocatalytic testing results.

3.7 Photocatalytic mechanism

The photocatalytic decomposition of RhB by using BiOCl g-C_3N_4, 20C_3N_4/ BiOCl systems were also investigated under different light irradiation. As depicted in Fig.7a, the photocatalytic

degradation for 20C_3N_4/ BiOCl systems under the irradiation of $\lambda \geq 532$ nm is lower than that of $\lambda \geq 420$ nm. As mentioned above, g-C_3N_4 can only be excited by the light with $\lambda < 455$nm (as shown in Fig.4). Hence, the photocatalytic activity of the g-C_3N_4/BiOCl composite system is mainly resulted from the BiOCl under $\lambda \geq 532$ nm irradiation. Considering that BiOCl cannot be excited by visible light because of its large energy band gap (3.21eV), the photosensitization would play an important role in the photo degradation of C_3N_4/BiOCl composite system.

To investigate the photocatalytic behaviours of C_3N_4/BiOCl photocatalysts, the photoinduced holes, superoxide radical and the hydroxyl radicals are selected for the oxidization of organic pollutants in aqueous media to reveal the photocatalytic mechanism. As can be seen from Fig.7b, the photodegradation of RhB for 20C_3N_4/BiOCl photocatalyst is significantly suppressed after the injection of scavenger for superoxide radicals (BQ) and holes (EDTA-2Na). On the contrary, only slight reduce is observed with the addition of hydroxyl radicals quencher (t-BuOH), indicating that the hydroxyl radicals are not the main oxidative species of this photocatalysts. Therefore, the superoxide radicals and holes would play a dominant role in visible-light-induced photocatalyst for C_3N_4/BiOCl composite system.

On the basis of experimental and theoretical results, a proposed mechanism for the enhanced C_3N_4/BiOCl photocatalyst is shown as below: When the composite photocatalyst is illuminated by visible light, BiOCl cannot be excited by visible light due to its large energy band gap. Nevertheless, both RhB and g-C_3N_4 would be excited and generate the photoinduced electron-hole pairs. Because the CB edge potential of g-C_3N_4 is more negative than that of BiOCl, the photoinduced electrons on the g-C_3N_4 surfaces get easily transferred to the CB of BiOCl through the intimately contacted interfaces, leaving the holes on the VB of g-C_3N_4. On the other hand, RhB adsorbed on the surface of BiOCl is photosensitized. Photoexcited electron from LUMO of RhB would also be injected to the CB of BiOCl, since the LUMO levels of RhB is more negative than the CB edge potential of BiOCl. In such a way, the photogenerated electrons are accumulated on the CB of BiOCl and holes on VB of RhB and g-C_3N_4, which induces the efficient separation of photoinduced electron-hole pairs. BiOCl with large surface area can not only enhance the adsorption of cationic dye of RhB but also form the interfaces with g-C_3N_4 which favour the photoinduced electron transfer. It is worth to note that the oxygen vacancies on the surface of the BiOCl photocatalyst work as active electron trap to capture the electrons and promote the separation of photogenerated electron-hole pairs.[34] Electrons accumulated on the CB of BiOCl transfer to the higher CB of BiOCl potential more negative than $E_0(O_2/O_2^{\cdot-})$=-0.046eV and then are scavenged by oxygen to form $O_2^{\cdot-}$, which can react with RhB molecules for degradation.[35] At the same time, the photoinduced holes on the VB of g-C_3N_4 can oxidize the RhB directly at g-C_3N_4 surface. As a result, the C_3N_4/BiOCl photocatalyst have increased photocatalytic activity.

4. Conclusions

In summary, a series of C_3N_4/BiOCl composite photocatalyst were prepared by a facile solvothermal process in the presence of

AG. AG acts as the structure-directing agent and helps the formation of nano-sized BiOCl particles. During the reaction process, nano-sized flower-like BiOCl is synthesized in the presence of AG, which favours the formation of the more ginterfaces between the two components for C_3N_4/BiOCl composite photocatalysts. RhB is chosen to evaluate the photocatalytic activity of as-prepared samples under visible light. The C_3N_4/BiOCl composite with proper proportion has excellent performance and $20C_3N_4$/BiOCl possessed the highest photocatalytic activity. The synergistic effect between C_3N_4 and BiOCl is elucidated, as proven by photocurrent measurement. Based on the experimental and theoretical results, a possible photodegradation mechanism related to the combination of photosensitization and photocatalyst is proposed. It is expected that our present work could provide useful information for the fabrication of other heterstructured nanocomposite.

Acknowledgements

Notes and references

[a] School of Materials Science and Engineering, Wuhan University of Technology, 188 Luoshi Road, Hubei, P. R. China. Fax: +86 27 87214521; Tel: +86 27 87866762; Email: leiliwen@whut.edu.cn,

[b] State key laboratory of advanced technology for materials synthesis and processing, Wuhan University of Technology, 188 Luoshi Road, Hubei, 430070, P. R. China. Email: shswhut@gmail.com

† Electronic Supplementary Information (ESI) available: [details of any supplementary information available should be included here]. See DOI: 10.1039/b000000x/
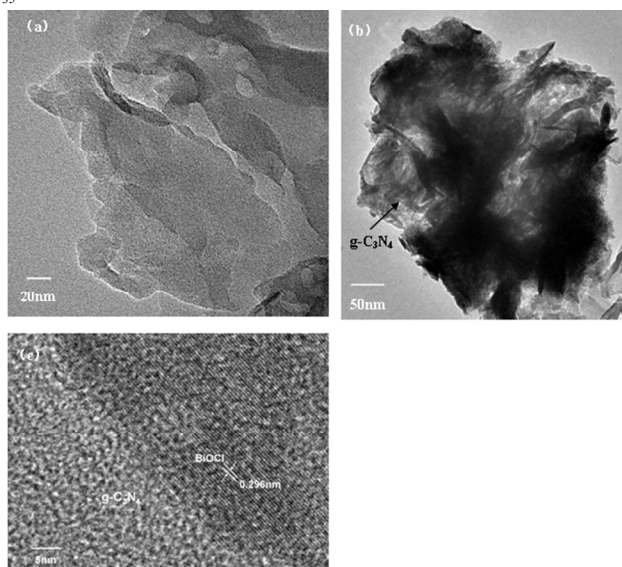

Fig.S1 HRTEM images of (a) g-C_3N_4 (b)(c) $20C_3N_4$/BiOCl photocatalysts
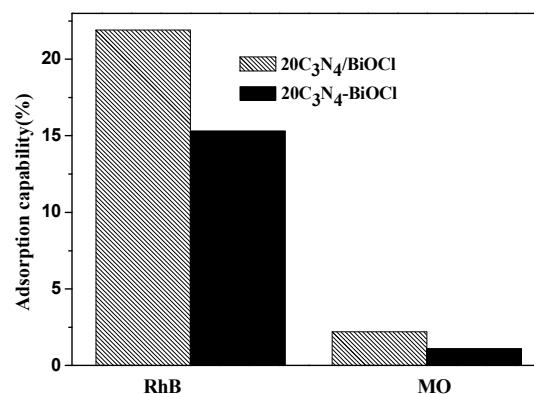

Fig.S2 Adsorption capability of RhB and MO over $20C_3N_4$/BiOCl and $20C_3N_4$-BiOCl photocatalysts

1   H. Tong, S.X. Ouyang, Y.P. Bi and N. Umezawa, *Adv. Mater.*, 2012, **24**, 229.

2   Y.S. Chen, J.C. Crittenden, S. Hackney, L. Sutter and D.W. Hand, *Environ. Sci. Technol.*, 2005, **39**, 1201.

3   F. Zuo, L. Wang, T. Wu, Z.Y. Zhang, D. Borchardt and P.Y. Feng, *J. Am. Chem. Soc.*, 2010, **132**, 11856.

4   L.P. Zhu, G.H. Liao, N.C. Bing, L.L. Wang, Y. Yang and H.Y. Xie. *CrystEngComm*, 2010, **12**, 3791.

5   K.L. Zhang, C. M. Liu, F.Q. Huang, C. Zheng and W.D. Wang, *Appl. Catal. B-Environ.*, 2006, **68**, 125.

6   X. Zhang , Z.H. Ai , F.L. Jia and L.Z. Zhang, *J. Phy. Chem.*, 2008, **112**, 747.

7   C.H. Wang, C.L. Shao, Y.C. Liu and L.N. Zhang, *Scripta Mater.*, 2008, **59**, 332.

8   J. Jiang , K. Zhao , X.Y. Xiao and L.Z. Zhang, *J.Am. Chem. Soc.*, 2012, **134**, 4473.

9   J. Jiang, L.Z. Zhang, H. Li, W.W. He and J.J. Yin, Nanoscale, 2013, 5, 10573.

10   K.Li, B. Chai, T.Y. Peng, J. Mao and L. Zan, *ACS Catal.*, 2013, **32**, 170.

11   L. Lin, Y.C. Yang, L. Men, X. Wang, D.N. He, Y.C. Chai, B. Zhao, S. Ghoshroy and Q.W. Tang, *Nanoscale*, 2013, **5**, 588.

12   S.Y. Chai, Y.J. Kim, M.H. Jung, A.K. Chakraborty, D.W. Jung and W.I. Lee, *J. Catal.*, 2009, **262**, 144.

13   Y.Y Li, J.S Wang, H.C. Yao, L.Y. Dang and Z.J. Li, *Catal. Commun.*, 2011, **12**, 660.

14   X.D. Zhang, X. Xie, H. Wang, J.J. Zhang, B.C. Pan and Y. Xie, *J. Am. Chem, Soc.*, 2013, **135**, 18.

15   G.S. Wu, S.S. Thind, J.L. Wen, K. Yan and A.C. Chen, *Appl. Cataly. B: Environ.*, 2013, **142-143**, 590.

16   X.C. Wang , S.F. Blechert and M. Antonietti, *ACS Cataly.*, 2012, **2**, 1596.

17   J.X. Sun, Y.P. Yuan, L.G. Qiu, X. Jiang, A.J. Xie, Y.H. Shen and J.F. Zhu, *Dalton Trans.*, 2012, **41**, 6756.

18   Y.J. Wang, X.J. Bai, C.S. Pan, J. He and Y.F. Zhu, *J. Mater. Chem.*, 2012, **22**, 11568.

19   K.I. Katsumata, R. Motoyoshi, N. Matsushita and K. Okada, *J. Hazard. Mater.*, 2013, **260**, 475.

20   C.S. Pan, J. Xu, Y.J. Wang, D. Li and Y.F. Zhou, *Adv. Funct. Mater.*, 2012, **22**, 1518.

21   X.J. Wang, Q. Wang, F.T. Li, W.Y. Yang, Y. Zhou, Y.J. Hao, S.J. Liu, *Chem. Eng. J.*, 2013, **234**, 361.

22   X. Chang, G. Yu, J. Huang, Z. Li, S. Zhu, P. Yu, C. Cheng, S.B. Deng and G.B. Ji, *Catal. Today*, 2010, **153**, 193.

23   Y.W. Zhang, J.H. Liu, G. Wu and W. Chen. *Nanoscale*, 2012, **4**, 5300.

24   Y.J. Wang, R. Shi, J. Lin and Y.F. Zhu, *Energy Environ. Sci.*, 2011, **4**, 2922

25 J. Di, J. X. Xia, S. Yin, H. Xu, M.Q. He, H.M. Li,. L. Xu and Y.P. Jiang. *RSC Adv.*, 2013, **3**, 19624.

26 D.H Wang, G.Q Gao, Y.W Zhang, L.S Zhou, A.W Xu and W. Chen, *Nanoscale*, 2012,**4**, 7780.

5 27 L. Ye, L. Zan, L. Tian, T. Peng, and J. Zhang, *Chem. Commun.*, 2011, **47**, 6951.

28 P.S Madhusudan, J.Y Yu, W.G Wang, B. Chenga and G. Liu, *Dalton Trans.*, 2012, **41**, 14345.

29 J. Wang and Y. Li, *Adv. Mater.*, 2003, **15**, 445.

10 30 Y.W Zhang, J.H Liu, G. Wu and W. Chen, *Nanoscale*, 2012, **4**, 5300.

31 J.X. Sun, Y.P. Yuan, L.G. Qiu , X. Jiang, A.J. Xie, Y.H. Shen and J.F. Zhu. *Dalton Trans.*, 2012, **41**, 6756.

32 L.M. Sun, X.Zhao, C.J. Jia, Y.X. Zhou, X.F. Cheng, P. Li, L. Liu and W.L Fan, *J. Mater. Chem.*, 2012, **22**, 23428.

15 33 X.P. Lin, F.Q. Huang, J.C. Xing, W.D. Wang and F.F. Xu, *Acta Materi.*, 2008, **56**, 2699.

34 M.A. Gondala, X. Chang, M.A. Ali, Z.H. Yamania, Q. Zhou and G. Ji, *Appl. Catal. A –Gen.*, 2011,**397**,192.; L.Ye, J. Chen, L. Tian, J. Liu, T. Peng, K. Deng and L. Zan, *Appl. Catal. B-Environ.*, 2013,

20 **130–131**, 1.

35 L.Q. Ye, J.Y. Liu, Z. Jiang, T.Y. Peng and L. Zan. *Appl. Catal. B-Environ.*, 2013, **142–143**, 1.; X.F. Chang, M.A. Gondal, A.A. Al-Saadi, M.A. Ali, H. Shen, Q. Zhou, J. Zhang, M.P. Du, Y.S. Liu and G.B. Ji. *J. Collid Interf. Sci.*, 2012, **377**, 291.

25

Graphical Abstract

Nanosized C_3N_4/BiOCl composite photocatalysts was synthesized via a facile solvothermal method in the presence of arabic gum. Arabic gum acts as the structure-directing agent and helps the formation of BiOCl nanoparticles with large specific surface area. A possible photocatalytic mechanism over C_3N_4/BiOCl composite photocatalysts is proposed by combing photosensitization and photocatalyst.
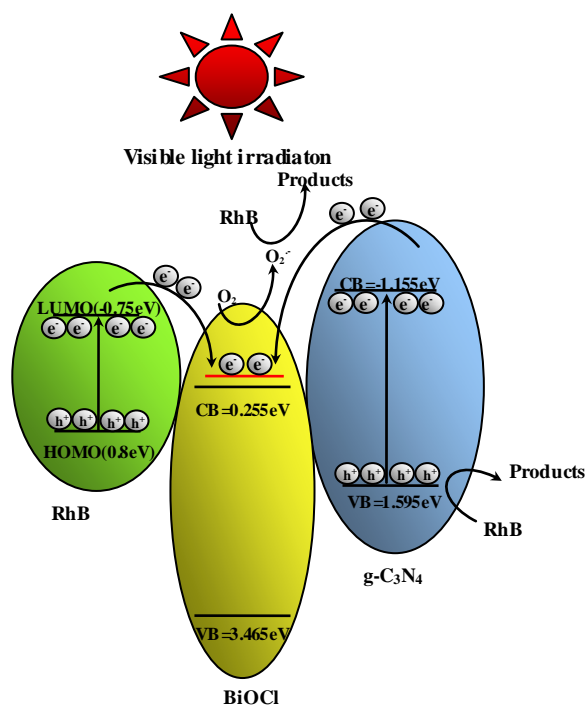
Abstract:

Nanosized C_3N_4/BiOCl composite photocatalysts was synthesized via a facile solvothermal method in the presence of arabic gum.The results indicate that arabic gum acts as the structure-directing agent and helps the formation of BiOCl nanoparticles. The more bonded interfaces may be produced between the two components for C_3N_4/BiOCl composite due to the synthesized BiOCl with the smaller size and the corresponding higher specific surface area. A significant enhancement of rhodamine B degradation is observed for the C_3N_4/BiOCl composite photocatalysts with proper proportion under visible light irradiation compared to pure C_3N_4 and BiOCl. The synergistic effect between C_3N_4 and nanosized BiOCl synthesized with the addition of arabic gum is elucidated, as proven by photocurrent measurement. Based on the calculated band position and the experimental results, the enhanced photodegradation could be attributed to the low recombination rate of the electron-hole pairs and the oxidation process of the generated superoxide radicals and holes. A possible photocatalytic mechanism over C_3N_4/BiOCl composite photocatalysts is proposed by combing photosensitization and photocatalyst.